

High stable photo-Fenton-like catalyst of FeP/Fe single atom-graphene oxide for long-term antibiotic tetracycline removal

Xiuying Li ^a, Jiayue Hu ^b, Yuepeng Deng ^a, Tong Li ^{a,c,*}, Zhao-Qing Liu ^d, Zhu Wang ^{a, **}

^a Institute of Environmental Research at Greater Bay/ Key Laboratory for Water Quality and Conservation of the Pearl River Delta, Ministry of Education, Guangzhou University, Guangzhou 510006, China

^b Department of Hygiene Inspection and Quarantine, School of Public Health, Anhui Medical University, Hefei 230032, China

^c Beijing Key Laboratory of Resource-oriented Treatment of Industrial Pollutants, School of Energy and Environmental Engineering, University of Science and Technology Beijing, Beijing 100083, China

^d School of Chemistry and Chemical Engineering/Institute of Clean Energy and Materials/Guangzhou Key Laboratory for Clean Energy and Materials, Guangzhou University, Guangzhou 510006, China



ARTICLE INFO

Keywords:

Photo-Fenton-like catalyst
Iron phosphide
Fe single atom-graphene oxide
Tetracycline degradation
Long-term stability

ABSTRACT

The Fenton-like reaction has always suffered from the disadvantages of narrow pH and poor stability. Herein, a Fenton-like catalyst with dual-photo-functional sites of iron phosphide (FeP) and Fe single atom-graphene oxide (Fe₁-GO) nanocomposite was constructed to activate H₂O₂ for antibiotic tetracycline (TC) pollutants removal. Under visible light irradiation, the degradation efficiency of TC reached 100 % within 30 min by FeP/Fe₁-GO was 1.36 and 2.32 times than single component of FeP and Fe₁-GO. Noteworthy, an extremely long-term stability with 100 times of recycling is achieved and the present system also bear a broad pH range with 3–11. The efficient charge separation and rich Fe single atoms active sites contribute the well Fe³⁺/Fe²⁺ cycles to support long-term multiple recycles. Finally, the TC degradation pathway and the toxicity of intermediate products were inferred. This work provides a way to construct high-stable Fenton-like catalyst via dual-photo-functional sites together with single atoms strategy.

1. Introduction

Tetracycline (TC), the second most used antibiotic class, is typically discharged directly into the water environment, posing a significant risk to human health and aquatic ecosystems [1]. Currently, various strategies including biodegradation [2], physical adsorption [3], and advanced oxidation processes (AOPs) [4] have been employed to remove and degrade TC in the aquatic environment. Among these, Fenton and Fenton-like process, as one of the primary techniques applied in AOPs, is a particularly powerful and environmentally friendly method [5]. The highly reactive hydroxyl radical (HO[•]) generated from the reaction of Fe²⁺ and H₂O₂ rapidly destroys the TC structure. Unfortunately, the conventional homogeneous Fenton reaction has significant limitations, including the inability to recycle Fe²⁺ [6,7], severe solution acidity (optimal pH = 2.0 ~ 4.0), and the production of substantial volumes of iron sludge as hazardous waste [8,9]. To solve these

flaws, lots of efforts have been invested in the creation of non-homogeneous Fenton systems that natural Fe minerals and Fe oxides have been employed to remediate refractory organic contaminants with a wide pH range [10–12]. However, the actual applications of monometallic iron compound catalysts (ZVI, Fe₂O₃, Fe₃O₄ and FeOOH) are limited since they have low catalytic activity, poor stability and recoverability [13–16].

Iron phosphide (FeP), differs from iron hydroxyl compounds in that the Fe has a partial positive charge (Fe^{δ+}, 0 < δ+ < 2), whereas the P has a partial negative charge (P^{δ-}, -1 < δ- < 0), making it significantly comparable to metallic Fe [15,16]. Consequently, both structural Fe^{δ+} and surface Fe²⁺ in FeP can provide electrons for catalytic oxidation [17–19]. Besides, the bandgap of FeP is around 1.1 eV [20] which means that it has broad light-harvesting ability to convert sunlight to chemical energy. These advantages make the FeP as the potential photo-Fenton-like catalyst. However, there are some problematic

* Corresponding author at: Institute of Environmental Research at Greater Bay/ Key Laboratory for Water Quality and Conservation of the Pearl River Delta, Ministry of Education, Guangzhou University, Guangzhou 510006, China.

** Corresponding author.

E-mail addresses: litong619@ustb.edu.cn (T. Li), wangzhu@gzhu.edu.cn (Z. Wang).

obstacles still hindering the future development of FeP in photo-Fenton-like reaction, including: (1) low electron conductivity, which hinders the rapid electron transfer within the catalyst and limits the reaction rate for degrading organic pollutants [21]; (2) the active sites on the surface of bulk FeP particles are insufficient, resulting in poor $\text{Fe}^{3+}/\text{Fe}^{2+}$ cycle, which lead an unsatisfactory of long-term cycling performance and stability [7].

Fe single-atom catalysts achieve the highest atom utilization and the exposure of catalytic sites, receiving more and more attentions in AOPs [22,23]. Fe single atoms mainly load on the carbon materials, wherein graphene oxide (GO) not only possesses rich oxygen functional groups to coordinate with Fe atoms to form single atom sites, but also has locally conjugated aromatic system to accelerate electron transfer. Moreover, GO also was demonstrated to be the visible light (Vis) photocatalyst in various photocatalytic applications [24]. These unique properties endow Fe single atom-graphene oxide (Fe₁-GO) with the great potential to be the photo-Fenton catalyst as well as the electrons internal transfer promotor to resolve the above limitations of FeP. Accordingly, combining FeP with Fe₁-GO, dual photo-functional sites of Fenton-like catalyst was constructed, and the purposes of this research are to: (i) evaluate the degradation efficiency of TC in FeP/Fe₁-GO/H₂O₂ system with and without visible light irradiation; (ii) evaluate the key practical parameters (pH and long-term stability) in Fenton-like reaction; (iii) reveal the degradation mechanism and electron transfer process in the FeP/Fe₁-GO/H₂O₂ system; (iv) elucidate the degradation pathway and intermediate products of TC.

2. Materials and methods

2.1. Chemicals

Iron nitrate hexahydrate ($\text{Fe}(\text{NO}_3)_3 \bullet 9 \text{ H}_2\text{O}$), ammonium phosphate ($(\text{NH}_4)_2\text{HPO}_4$), tetracycline hydrochloride, hydrogen peroxide (H_2O_2), dimethyl sulfoxide (DMSO) and methanol were obtained from Sino-pharm Chemical Reagent Co. Ltd. (China). 2,2,6,6-tetramethyl-4-piperidino (TEMP), 5,5-dimethyl-1-pyrroline N-oxide (DMPO) were purchased from Sigma-Aldrich. Graphene oxide (GO) was purchased from Xianfeng Nano Material Technology Co., Ltd. The remaining reagents were analytical grade and did not require additional purification.

2.2. Synthesis of FeP catalysts

Firstly, 9.67 g of $\text{Fe}(\text{NO}_3)_3 \bullet 9 \text{ H}_2\text{O}$ and 5.28 g of $(\text{NH}_4)_2\text{HPO}_4$ were dissolved in distilled water (DIW) to form solutions A and B, respectively. Then, solution B was added into solution A drop by drop with vigorous stirring for 2 h. The solution was placed on an electric stove to evaporate the water and dried at 120 °C overnight. Finally, the FeP precursor was obtained by roasting at 550 °C for 3 h.

The FeP precursors were pressed into sheets at a pressure of 20 MPa and crushed to 20–40 mesh. The voltage of the high-voltage electrode was maintained at around 8.0 kV under H_2 protection for 2 h. Finally, passivation was carried out under 0.5 % O_2/He for 2 h, resulting in the final product of FeP.

2.3. Synthesis of Fe₁-GO single atom catalysts

40 mg GO and 10 mg $\text{Fe}(\text{NO}_3)_3 \bullet 9 \text{ H}_2\text{O}$ were dissolved in 20 mL of DIW to obtain solutions A and B, respectively. Solution B was slowly added into solution A and the mixture was stirring at 150 rpm for 24 h. Then, the solution was separated by centrifugation at 14,000 rpm and washed for 4 times, and finally freeze-dried to obtain Fe₁-GO single atom catalysts.

2.4. Synthesis of FeP/Fe₁-GO nanocomposites

The FeP/Fe₁-GO composites were obtained by electrostatic

attraction-impregnation composite method. In brief, 50 mg FeP and different amounts Fe₁-GO were added into 20 mL DIW, and the mixture was stirring by magnetic stirrer at 150 rpm for 12 h. Then, the powders were obtained by centrifugation at 14,000 rpm and washed for 4 times to obtain the final products of FeP/Fe₁-GO. The number of Fe₁-GO accounts for 5 %, 10 %, 15 % and 20 % of the total mass in this procedure, respectively.

2.5. Instrumentation and characterization

The morphologies of samples were measured via transmission electron microscopy (TEM, JEOL, JEM-2100 F). High-angle annular dark-field (HAADF) images were acquired with a JEM-ARM200F TEM/STEM with a spherical aberration corrector working at 300 kV. The phase was carried out using X-ray diffraction (XRD, Rigaku Ultima IV). The local structures of samples were characterized by X-ray photoelectron spectroscopy (XPS, ESCALAB 250 photoelectron spectrometer, Thermo-VG Scientific) and Raman spectra (LabRAM HR Evolution, HORIBA Jobin Yvon S.A.S., France). A UV-vis-near-infrared (UV-Vis-NIR) spectrophotometer (JASCO V770 spectrophotometer) was used to investigate the absorption of samples. The content of Fe in the as-prepared catalysts was examined by an inductively coupled plasma atomic emission spectrometer (ICP-OES, EXPEC 6500). X-ray absorption near-edge structure (XAFS) and extended X-ray absorption fine structure (EXAFS) data were obtained at the beamline BSRF station of the Beijing Synchrotron Radiation Facility, China.

2.6. Experimental procedure and analysis methods

Every experiment was carried out in a 50 mL quartz beaker. A 300 W xenon light source (PLS-SXE300D, Beijing Perfectlight Technology Co., Ltd) with a 400 nm cut-off filter served as the light source (light intensity: 150 mW cm^{-2}). First, FeP/Fe₁-GO powder was added to the solution and agitated for 30 min to completely scatter the catalyst and achieve adsorption equilibrium. Then, the degradation reaction was started by adding H_2O_2 while the light source was turned on. The FeP/Fe₁-GO dose, H_2O_2 concentration, and beginning concentration TC were 0.15 g/L, 0.1 M, and 0.01 g/L, respectively. Next, the reaction was then quenched by adding an excess of $\text{Na}_2\text{S}_2\text{O}_3$ to 1 mL of the reaction solution at preset times. The pseudo-first-order kinetics model was used to express the reaction kinetics of TC degradation, which is calculated using the following equation:

$$\ln(C_0/C_t) = kt \quad (1)$$

where k represents the rate constant (min^{-1}) of TC degradation; t is the reaction time (min); and C_0 and C_t represent the concentration of TC (mg L^{-1}) at times 0 and t , respectively. The material was then immediately filtered via a 0.22 μm filter before being analyzed using high-performance liquid chromatographic techniques (HPLC, Shimadzu, LC-16). The mobile phases were acetonitrile and 0.1 % formic acid in a 15 %: 85 % in water, and the HPLC was fitted with a diode array detector at 365 nm. The degradation products were identified by a liquid chromatography/time-of-flight/mass spectrometer (LC-TOF-MS, AB Sciex, LC-Triple-TOF5600) in positive mode (ESI+). The mass spectrum was scanned in positive ion mode across a 50–600 m/z range. Gradient elution with 0.10% formic acid water as mobile phase A and acetonitrile as mobile phase B was used in the tests. The gradient elution process was as follows: increase acetonitrile from 5 % to 65 % over 5 min and hold for 10 min, then decrease acetonitrile to 5 % over 5 min. Analyst® software was used to calculate the concentrations of TC and degradation products.

Electron paramagnetic resonance (EPR) spectra equipped with DMPO or TEMP as the spin-trapping agent were detected on a Bruker spectrometer (ESR Nano) in water or dimethyl sulfoxide solution. The electrochemical measurements were carried out in the quartz beaker via

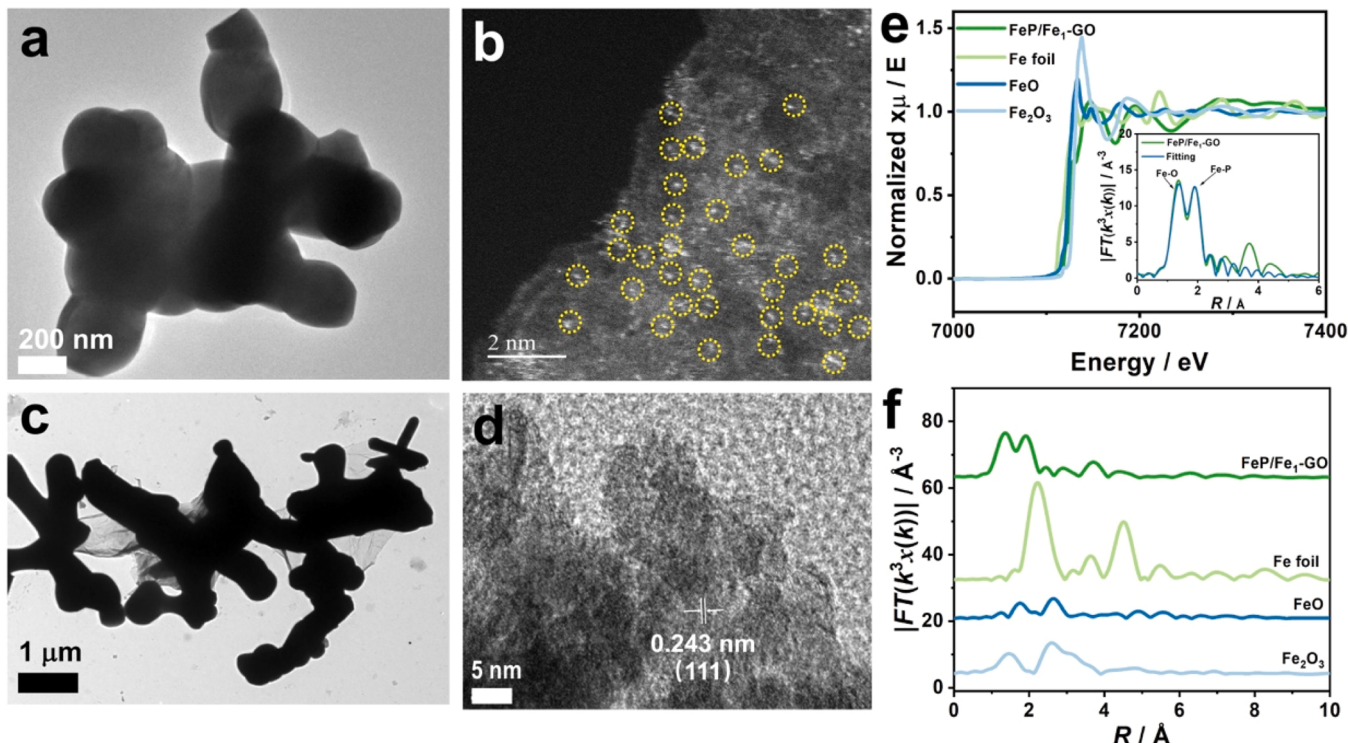


Fig. 1. TEM images of FeP (a) and FeP/Fe₁-GO (c), AC HAADF-STEM image of Fe₁-GO (b), (d) HRTEM image of FeP/Fe₁-GO nanocomposites. (e) Normalized Fe K-edge XANES spectra of FeP/Fe₁-GO, Fe₂O₃, and reference Fe foil the corresponding fitting curve for the FeP/Fe₁-GO (e inset). (f) Fourier-transform EXAFS spectra of FeP/Fe₁-GO and Fe foil.

an electrochemical workstation CHI 760E (Shanghai Chenhua Instrument Co., Ltd., China) with three electrodes system, wherein the FeP, Fe₁-GO or FeP/Fe₁-GO modified glassy carbon electrode (GCE) was

acted as working electrode. Pt wire and Ag/AgCl (3.5 M KCl) electrode were acted as counter and reference electrodes, respectively. The detail electrochemical measurement procedure available in [Supporting](#)

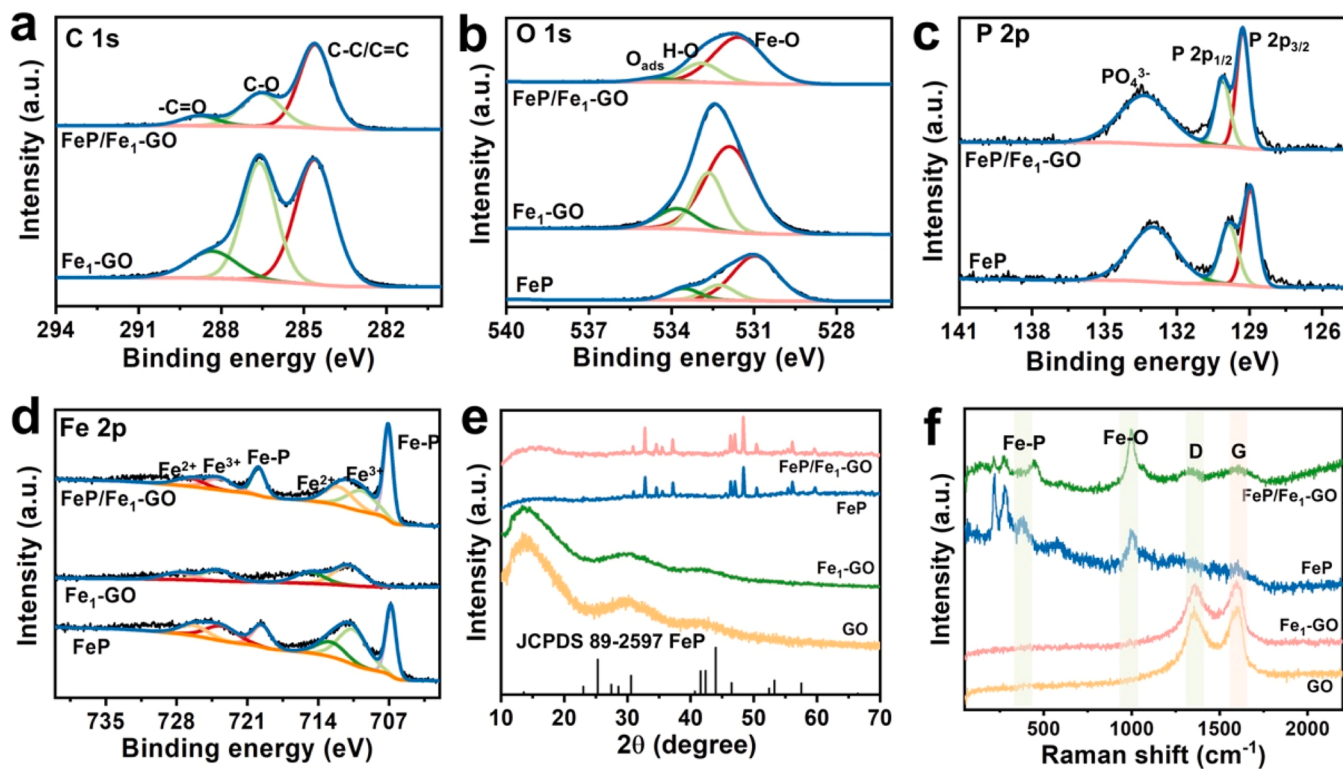


Fig. 2. XPS spectra of (a) C 1 s; (b) O 1 s; (c) P 2p and (d) Fe 2p for FeP, Fe₁-GO and FeP/Fe₁-GO; (e) XRD patterns and (f) Raman spectra of FeP, Fe₁-GO and FeP/Fe₁-GO.

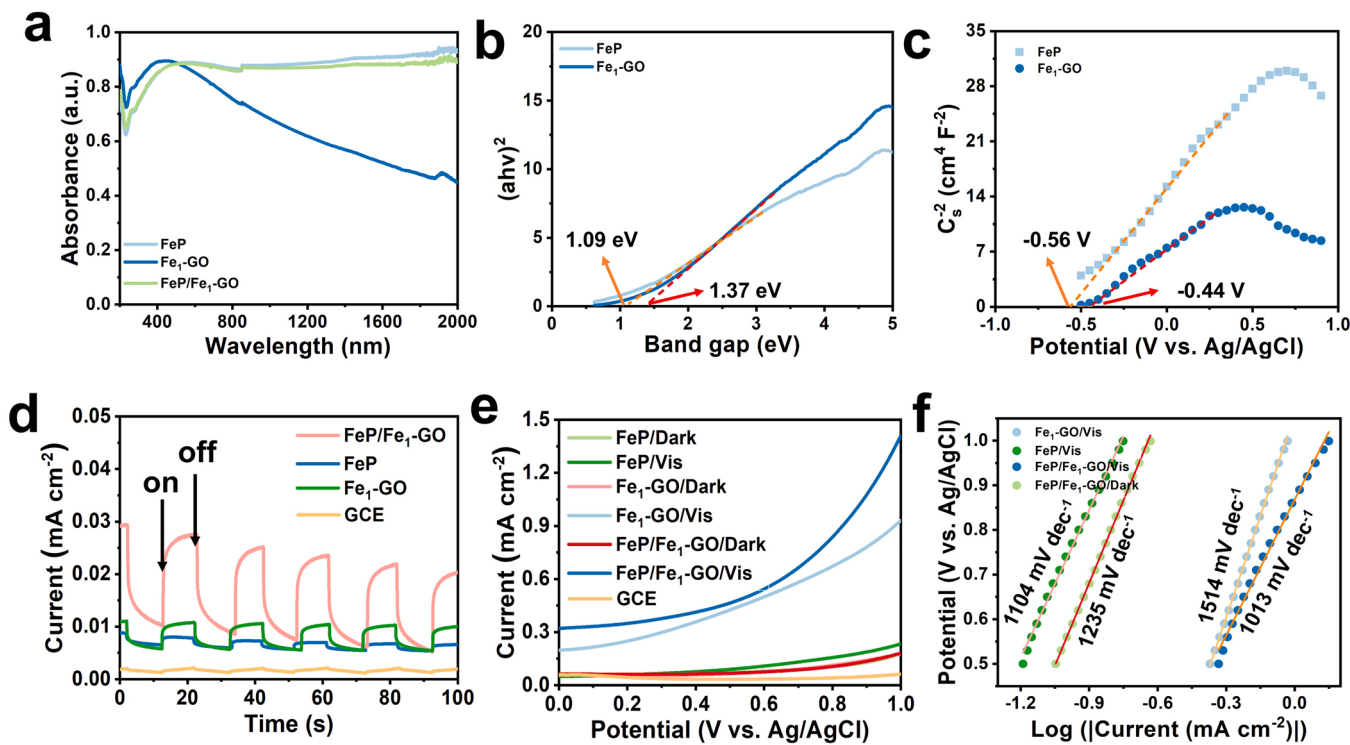


Fig. 3. (a) UV-Vis-NIR spectra of FeP, Fe₁-GO and FeP/Fe₁-GO; (b) Bandgap energy and (c) Mott-Schottky plots of FeP and Fe₁-GO; (d) Photocurrent responses of Fe₁-GO, FeP and FeP/Fe₁-GO in 0.5 M Na₂SO₄ solution; (e) Linear sweep voltammetry (LSV) and (f) Tafel slope curves of Fe₁-GO, FeP and FeP/Fe₁-GO in 0.5 M Na₂SO₄ solution under dark and visible light irradiation condition.

Information.

3. Results and discussion

3.1. Characterization

TEM and aberration-corrected high-angle annular dark-field scanning transmission electron microscopy (AC HAADF-STEM) were performed to elucidate the microstructure of the samples. As shown in Fig. 1a, FeP has a roughly polyhedral structure with irregular shape and uniform size distribution. For Fe₁-GO, the isolated and dense brilliant spots seen in HAADF-STEM measurements suggest the production of single Fe atoms (Fig. 1b). As shown in Fig. 1c, clear irregular FeP and sheet-like Fe₁-GO are observed, proving the successful synthesized FeP/Fe₁-GO nanocomposite. From HRTEM image (Fig. 1d), the typical lattice fringes of FeP with the interplanar spacings of 0.243 nm are corresponded to the (111) plane of FeP in the FeP/Fe₁-GO [25,26].

XANES and EXAFS spectra were examined to understand more about the electronic structure and coordination environment of individual Fe atoms in FeP/Fe₁-GO. A nearly identical absorption edge to that of Fe₂O₃ was evident in the XANES spectra of Fe in FeP/Fe₁-GO (Fig. 1e), showing that Fe was in a positive valence state close to + 3. The best fit of the first shell shows that the Fe atoms were coordinated by O atoms on average 2-folds (Fig. 1e insert, Supplementary Table S1). The Fe-O scattering channel was shown as a strong peak at 1.44 Å in the Fourier transform EXAFS spectra of FeP/Fe₁-GO (Fig. 1f). The coordination structure surrounding the Fe core is further validated by the curve fit of the EXAFS data of FeP/Fe₁-GO. It is worth noting that the loading mass of a Fe single atom on the graphene surface was 4.1 wt% by the ICP test.

The surface chemical composition and states of FeP, Fe₁-GO, and FeP/Fe₁-GO were depicted by XPS, as seen in Fig. 2a-d. Three peaks that correspond to graphene oxide and adsorbed CO₂ in the catalyst were found at binding energies of 288.3 eV (-C=O), 286.6 eV (C-O) and 284.6 eV (C-C or C=C), respectively, in the C1s spectrum (Fig. 2a). The

O 1s spectra (Fig. 2b) of samples represents adsorbed oxygen (533.8 eV), H-O (532.7 eV) and Fe-O (531.9 eV) [27]. The phosphide signal at 129.8–130.7 eV in Fig. 2c provides additional support for the synthesis of FeP and FeP/Fe₁-GO. The phosphorus oxide was the source of the peak at 133.0 eV in the P 2p spectra [28]. The XPS spectra of Fe 2p are shown in Fig. 2d. There are six significant peaks that are ascribed to Fe²⁺, Fe³⁺ and Fe-P at 726.3, 723.5, 719.6, 712.8, 710.6 and 706.7 eV, which demonstrate the creation of FeP, Fe₁-GO, and Fe-P/Fe₁-GO as well as potential iron oxides from air oxidation [29,30]. Note that, the elemental binding energy in FeP/Fe₁-GO was shifted with respect to FeP and Fe₁-GO. These results suggest a strong electronic interaction between FeP and Fe₁-GO, which is important for regulating the catalytic ability of the catalyst.

XRD patterns of GO, FeP, Fe₁-GO and FeP/Fe₁-GO are shown in Fig. 2e. The diffraction peaks of Fe₁-GO were essentially the same of pure GO, no peaks were observed except for a diffraction peak attributed to GO at 13.4°, indicating that Fe did not form iron monomers or oxides on GO, therefore existed as iron single atoms [31]. For FeP, the XRD diffraction peaks corresponded well to the orthogonal FeP (JCPDS 89-2597), indicating the successful preparation of FeP [32]. The FeP/Fe₁-GO pattern had not significantly different from FeP, while no GO peaks are observed, which may be due to the low amount of Fe₁-GO or weak GO diffraction peaks [33]. The Raman spectra of FeP/Fe₁-GO revealed bonds associated with Fe-P (Fe-P [366.9 cm⁻¹] and Fe-O [994.5 cm⁻¹]) [34] and graphitic carbon (D-band [1359 cm⁻¹] and G-band [1579 cm⁻¹]) [35] further demonstrating the formation of FeP/Fe₁-GO (Fig. 2f). The weak peak intensity of carbon indicates a thin carbon layer, which closely agrees with the TEM and XRD observations. In addition, the D and G band intensity ratio of FeP/Fe₁-GO ($I_D/I_G \approx 0.99$) was higher than that of Fe₁-GO ($I_D/I_G \approx 0.97$). The FTIR spectra also demonstrated the successful preparation of FeP/Fe₁-GO nanocomposites (Fig. S1). This implies the presence of additional defects and pores in the carbon of FeP/Fe₁-GO, leading to the exposure of additional active sites that are responsible for the enhanced catalytic activity [36].

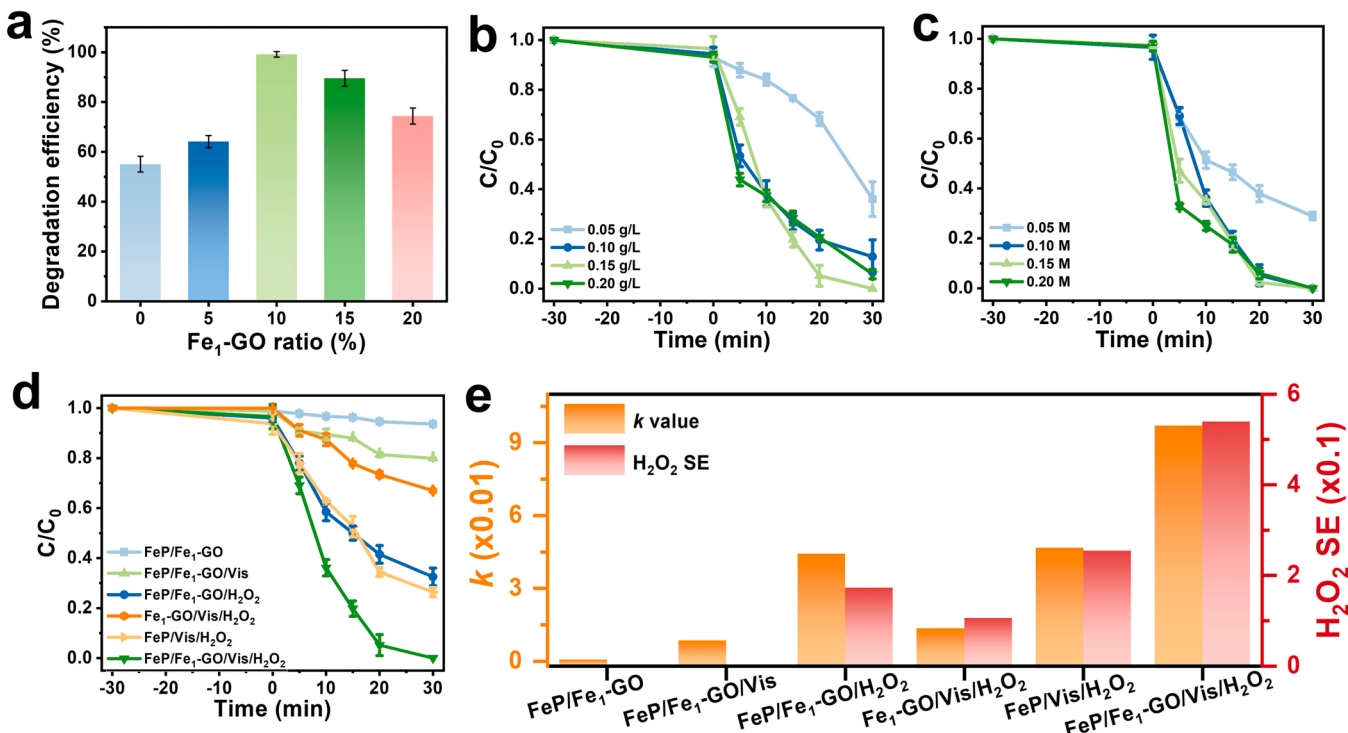


Fig. 4. (a) Degradation efficiency of TC for different mass ratios of Fe₁-GO in FeP/Fe₁-GO with H₂O₂ and visible light irradiation. TC degradation in different dosage of catalyst (b) and H₂O₂ (c) in FeP/Fe₁-GO/Vis/H₂O₂ system. (d) TC degradation under different oxidation systems. (e) Pseudo-first order kinetics value and H₂O₂ SE of TC degradation under different oxidation systems.

3.2. Optical and photoelectric properties

The UV-Vis-NIR spectra of FeP, Fe₁-GO, and FeP/Fe₁-GO were measured to investigate respective optical absorption characteristics. In Fig. 3a, it can be shown that FeP, Fe₁-GO and FeP/Fe₁-GO exhibit a wide range of absorption from the UV to the NIR region, suggesting that the produced FeP/Fe₁-GO has potential photoresponse capacity under visible light. According to the Tauc/Davis-Mott model, the bandgap (E_g) values for FeP and Fe₁-GO were 1.09 and 1.37 eV (compared to the normal hydrogen electrode (relative to the NHE)), respectively (Fig. 3b). As shown in Fig. 3c, the Motte-Schottky plots with positive slopes demonstrated that FeP and Fe₁-GO possesses n-type semiconductor characteristic and the E_{fb} was determined at -0.56 and -0.44 V for FeP and Fe₁-GO (versus Ag/AgCl), respectively. The E_{fb} of FeP and Fe₁-GO were further transformed into -0.36 and -0.24 V using the equation $E_{NHE} = E_{Ag/AgCl} + 0.197$ V. (vs. NHE). Because E_{fb} was about 0.1 eV higher than the conduction band potentials (E_{CB}) of n-type semiconductor, the E_{CB} of FeP and Fe₁-GO were roughly calculated to be -0.46 and -0.34 V (vs. NHE), respectively, and the valence band (VB) positions of FeP and Fe₁-GO were roughly calculated to be 0.63 and 1.03 V (vs. NHE), respectively [37].

As is commonly known, a key determinant of the effectiveness of photocatalysis was the separation efficiency of photogenerated charges. The highest current response (0.023 mA cm⁻²) was obtained when FeP/Fe₁-GO under visible light irradiation, superior to GCE, FeP or Fe₁-GO alone under visible light irradiation (Fig. 3d), implying that FeP/Fe₁-GO has the ability of rapid charge separation [38–40]. To investigate the photocatalytic properties of GCE, FeP, Fe₁-GO, and FeP/Fe₁-GO complexation, we further performed electrochemical characterization. The blank GCE electrode has the lowest current intensity, and the current intensity of the working electrode was improved after catalyst modified. Under visible light irradiation, the current intensity of FeP and Fe₁-GO (Fig. 3e) increased to 0.23 and 0.93 mA cm⁻² at a bias voltage of 1.0 V, respectively, verifying that FeP and Fe₁-GO can respond to visible

light and generate surface charges. In addition, after modification with Fe₁-GO, a highest current intensity (1.39 mA cm⁻²) was obtained at the bias voltage of 1.0 V. These results suggested that Fe₁-GO as an excellent electron conductor accelerate the photogenerated electron transfer process. Therefore, the photocatalytic activity of FeP is improved by Fe₁-GO composite. The photocatalytic reaction kinetics of FeP, Fe₁-GO and FeP/Fe₁-GO under visible light irradiation were evaluated by Tafel analysis (Fig. 3f). The Tafel slope of FeP/Fe₁-GO nanocomposites under visible light was much smaller than that under FeP and Fe₁-GO, which indicated that the Fe₁-GO composite could effectively improve the photocatalytic performance of FeP.

3.3. Photo-Fenton-like reaction to remove TC

To investigate the optimum weight ratio of Fe₁-GO in the composites of FeP/Fe₁-GO, different weight ratios (0–20 %) of Fe₁-GO in the FeP/Fe₁-GO degradation TC under FeP/Fe₁-GO/Vis/H₂O₂ system were carried out. As shown in Fig. 4a, the degradation efficiency of TC in the FeP/Fe₁-GO/Vis/H₂O₂ system showed an increase and then a decrease with the continued increase of Fe₁-GO amount, and the optimal weight ratio of Fe₁-GO was about 10 %. Then, the effects of reaction parameters, including catalyst and H₂O₂ dosages, on H₂O₂ activation of TC degradation were further investigated. First, the amount of catalyst was adjusted to degrade TC in the FeP/Fe₁-GO/Vis/H₂O₂ system (Fig. 4b). Within 30 min, the TC degradation rate went from 63.9 % to 100 % when the FeP/Fe₁-GO concentration was raised from 0.05 to 0.2 g/L. The catalyst concentration of 0.15 g/L was the most favorable for the degradation of TC. Secondly, the concentration of 0.1–0.2 M H₂O₂ could effectively remove TC (Fig. 4c), while 0.05 M H₂O₂ is insufficient. It can be seen that the degradation of TC was significantly enhanced when the H₂O₂ concentration increased from 0.05 M to 0.1 M, and the degradation efficiency of TC was mostly consistent when the H₂O₂ concentration increased from 0.1 to 0.2 M. Therefore, the H₂O₂ concentration was set to 0.1 M to accommodate both efficient removal and cost reduction

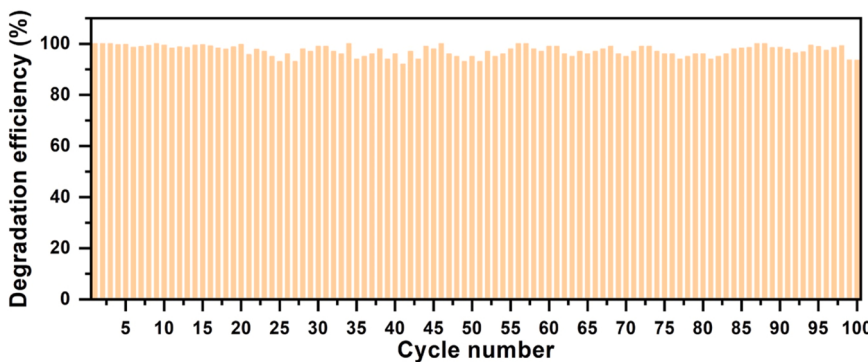


Fig. 5. Reusability tests of FeP/Fe₁-GO/Vis/H₂O₂ with successive 100-time runs.

ranges.

As described above, the optimal reaction conditions were determined to be 0.15 g/L FeP/Fe₁-GO and 0.1 M H₂O₂. The efficiency of visible light, Fe₁-GO and FeP alone in activating H₂O₂ for TC degradation was 7.3 %, 26.5 % and 34.4 %, respectively. (Fig. S2). In contrast, individual FeP/Fe₁-GO, FeP/Fe₁-GO/Vis, FeP/Fe₁-GO/H₂O₂, FeP/Vis/H₂O₂, and Fe₁-GO/Vis/H₂O₂ systems were also used to degrade TC (Fig. 4d). After the reaction for 30 min, almost all TCs in the FeP/Fe₁-GO/Vis/H₂O₂ system was degraded (100 %), while the efficiency of TC degradation in the FeP/Fe₁-GO, FeP/Fe₁-GO/Vis, FeP/Fe₁-GO/H₂O₂, FeP/Vis/H₂O₂ and Fe₁-GO/Vis/H₂O₂ systems were 6.4 %, 20.1 %, 67.5 %, 73.7 % and 43.1 %, respectively. The degradation efficiency of TC by FeP/Fe₁-GO was 1.36 and 2.32 times than single component of FeP and Fe₁-GO. It is obvious that the FeP/Fe₁-GO/Vis/H₂O₂ system exhibits the most excellent ability to degrade TC. This was attributed to a synergistic effect between FeP and Fe₁-GO when activating H₂O₂ with FeP/Fe₁-GO nanocomposites. To confirm this, a pseudo-first-order kinetics analysis and the H₂O₂ stoichiometric efficiency (SE) were shown in Fig. 4e. The FeP/Fe₁-GO/Vis/H₂O₂ system reached the highest reaction rate constant ($k = 0.097 \text{ min}^{-1}$), which was about 1.07 times higher than that of

FeP/Vis/H₂O₂ and Fe₁-GO/Vis/H₂O₂ systems in sum. In order to further insights, the H₂O₂ utilization as the H₂O₂ stoichiometric efficiency (H₂O₂ SE) was calculated by correlating the H₂O₂ decomposition and TC degradation performance of all system following the Eq. (2), where $\Delta[\text{TC}]$ and $\Delta[\text{H}_2\text{O}_2]$ are the total decomposed amounts of TC and H₂O₂, respectively.

$$\text{H}_2\text{O}_2 \text{ SE} = \frac{\Delta[\text{TC}]}{\Delta[\text{H}_2\text{O}_2]} \quad (2)$$

Similarly, the FeP/Fe₁-GO/Vis/H₂O₂ system has the highest H₂O₂ SE (0.53), which is 2.1 and 4.9 times higher than the FeP/Vis/H₂O₂ and Fe₁-GO/Vis/H₂O₂ systems, respectively. Therefore, it is concluded that the excellent degradation of TC by the FeP/Fe₁-GO/Vis/H₂O₂ system was attributed to the synergistic effect between FeP and Fe₁-GO under visible light irradiation.

3.4. Long-term stability

The traditional homogeneous Fenton reaction has limited its application because of its not reusable. To investigate the stability of FeP/Fe₁-

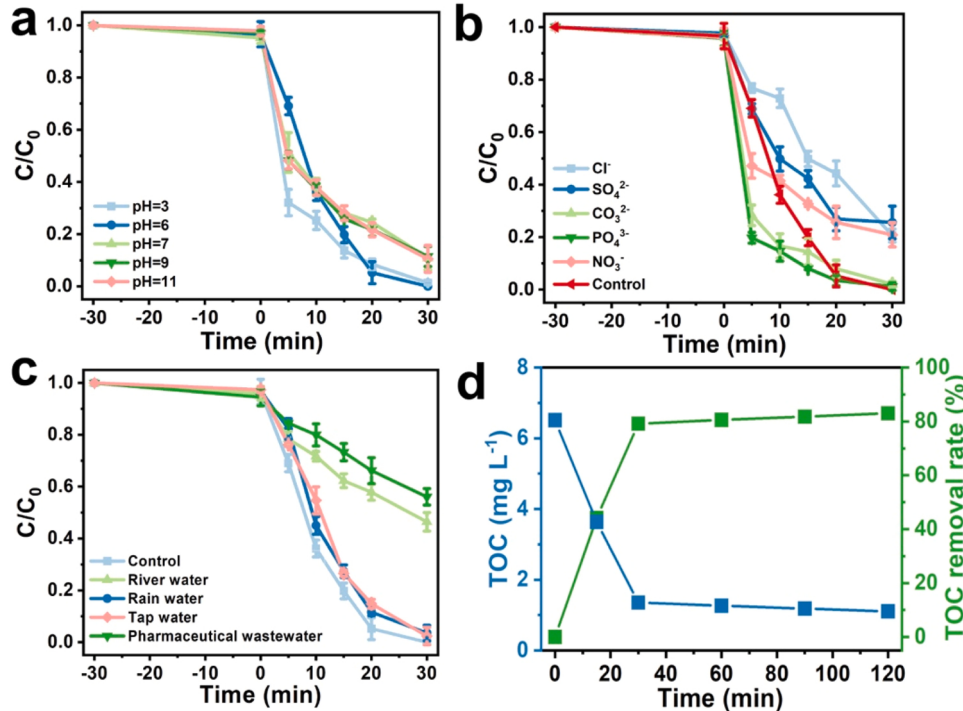


Fig. 6. Influence of initial solution pH (a), inorganic anions (b), different water matrices (c) on TC degradation by the FeP/Fe₁-GO/Vis/H₂O₂ system. (d) TOC concentration and TOC removal rate of TC degradation in FeP/Fe₁-GO/Vis/H₂O₂ system.

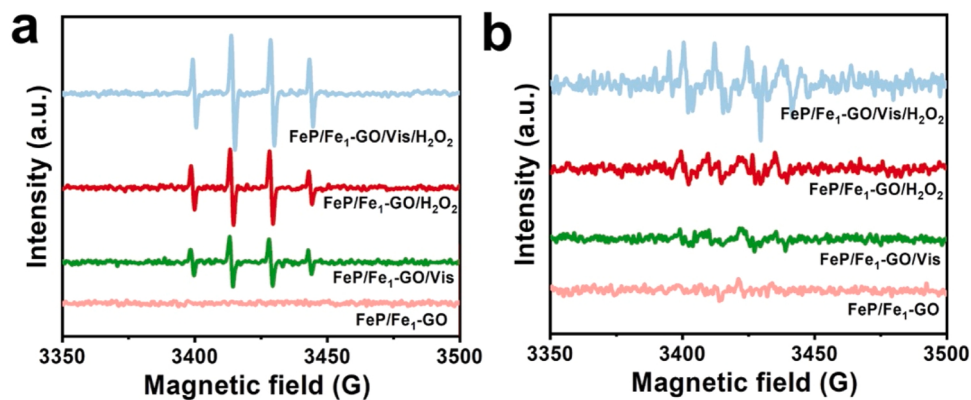


Fig. 7. EPR spectra of different samples and conditions by DMPO-HO[•] in DIW solution (a), EPR spectra by DMPO-O₂^{•-} in methanol solution (b).

GO, the recycle degradation process of TC by using FeP/Fe₁-GO/Vis/H₂O₂ system was investigated. After the first run reaction, new solutions of TC pollutants and H₂O₂ were added into the next round reaction. As shown in Fig. 5, the as-prepared FeP/Fe₁-GO catalysts kept very stable and each round of TC were quickly degraded. Interestingly, the whole degradation process can maintain more than 100 times. The degradation efficiency of the FeP/Fe₁-GO/Vis/H₂O₂ system for TC even remained at about 93.6 % after 100 cycles. In addition, the ions of Fe content in the system was kept at a low concentration (Fig. S3) during this long-term recycle reactions. This excellent long time cycling performance may be because of the rapid charge transfer and well Fe³⁺/Fe²⁺ cycles in the FeP/Fe₁-GO/Vis system, which will discuss in the following section in detail.

3.5. Practical application parameters for TC degradation

To investigate the effect of initial pH on TC degradation, the pH of TC solution was adjusted to 3.0, 6.0, 7.0, 9.0 and 11.0, respectively. As seen in Fig. 6a, the TC removal efficiencies were almost same at all pH condition by using FeP/Fe₁-GO as the photo-Fenton-like catalyst under visible light condition. These results show that FeP/Fe₁-GO/Vis/H₂O₂ system kept high performance at a wide pH environment. In addition, the effects of common inorganic anions such as Cl⁻, SO₄²⁻, CO₃²⁻, PO₄³⁻, and NO₃⁻ in wastewater on the FeP/Fe₁-GO/Vis/H₂O₂ system were investigated for practical applications. As shown in Fig. 6b, the effects of CO₃²⁻, PO₄³⁻ on TC degradation in the FeP/Fe₁-GO/Vis/H₂O₂ system are

negligible. In contrast, Cl⁻, SO₄²⁻ and NO₃⁻ showed weak inhibition on TC degradation, which could be either because of their low reactivity towards HO[•], or may be because by generation of secondary radicals like Cl[•], or most of the SO₄²⁻ is readily reduced to SO₃²⁻ by electrons. Therefore, the addition of Cl⁻, SO₄²⁻ and NO₃⁻ to the solution will compete with the HO[•] and O₂^{•-} generated by the FeP/Fe₁-GO/Vis/H₂O₂ system, thus inhibiting the TC degradation [41–43].

The TC degradation experiments have been conducted in different water environment including river water, rain water, tap water and pharmaceutical wastewater. Fig. 6c shows that about 53.6 %, 97.2 %, 97.6 % and 43.9 % of TC were removed within 30 min for the above water environment by using FeP/Fe₁-GO/Vis/H₂O₂ process, respectively. Although the performance is not as good as that of deionized water, this result confirms the great potential of the FeP/Fe₁-GO/Vis/H₂O₂ system for practical wastewater treatment. Fig. 6d shows the total organic carbon (TOC) concentration and TOC removal rate of FeP/Fe₁-GO/Vis/H₂O₂ system, which reached 79.2 % of TOC removal in the system within 30 min, further reaction up to 120 min did not significantly increase the mineralization rate. It may be due to the formation of difficult-to-degrade intermediates in the reaction. Therefore, this system has potential for practical water treatment application as it can solve the problems of narrow pH adaptation range, non-reusability and iron sludge generation of traditional Fenton reaction.

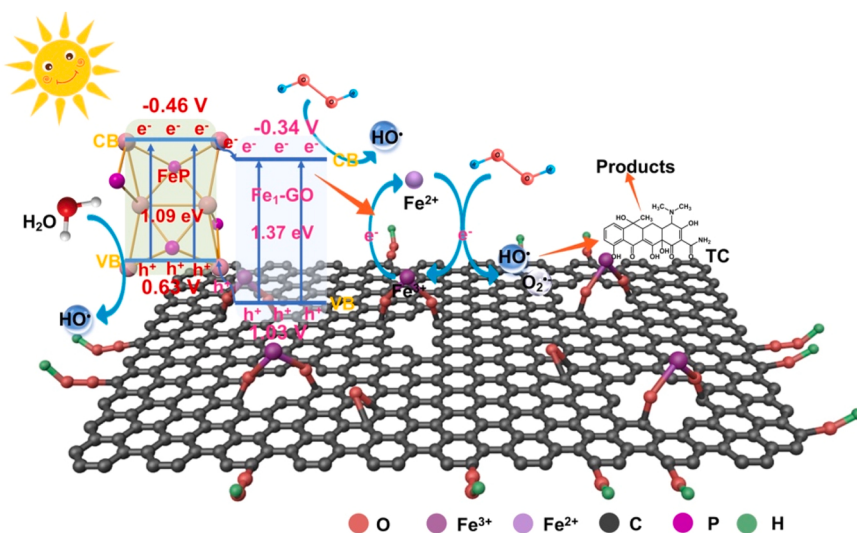


Fig. 8. Proposed synergistic mechanism of the FeP/Fe₁-GO/Vis/H₂O₂ system for TC degradation.

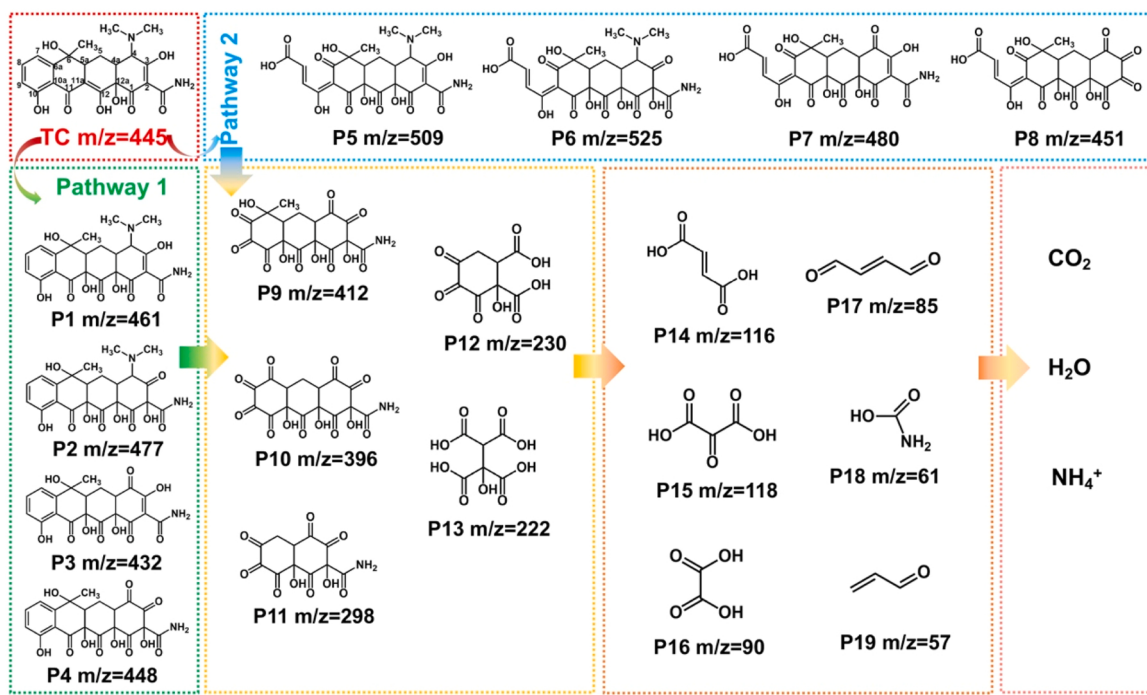


Fig. 9. Possible pathway of TC degradation in FeP/Fe₁-GO/Vis/H₂O₂ system.

3.6. Mechanism of FeP/Fe₁-GO/Vis/H₂O₂ system for TC degradation

In order to provide insight into TC degradation mechanism, it is important to determine which active species are responsible for TC degradation. The presence of active species in the FeP/Fe₁-GO/Vis/H₂O₂ system was demonstrated by EPR spectroscopy. Fig. 7a shows that when DMPO was employed as a scavenger to identify HO[•], a distinct signal of DMPO-HO[•] adducts was detected. When methanol was applied as a medium, weak signals belonging to DMPO-O₂^{•-} adducts were also observed (Fig. 7b). No signal of free radicals was detected for FeP/Fe₁-GO alone. In contrast, FeP/Fe₁-GO showed signals of similar species under both H₂O₂ alone and visible light conditions. The difference was that the corresponding signals of the FeP/Fe₁-GO/Vis/H₂O₂ system were significantly stronger than both FeP/Fe₁-GO/Vis and FeP/Fe₁-GO/H₂O₂, which also indicated that the activation of H₂O₂ by FeP/Fe₁-GO could be effectively enhanced under visible light irradiation. However, the weaker signal of O₂[•] compared to HO[•] may be due to the fact that the photogenerated electrons are more used for conversion of Fe³⁺ to Fe²⁺ rather than O₂ to O₂[•]. In order to prove the conversion of Fe³⁺ to Fe²⁺, the XPS spectra of Fe 2p of fresh and used FeP/Fe₁-GO catalyst were investigated (Fig. S4). For fresh catalysts, the pre-reaction percentages of Fe³⁺ and Fe²⁺ were 77.2 % and 22.8 %, respectively. For used catalysts, the percentages of Fe³⁺ and Fe²⁺ after the reaction were 67.9 % and 32.1 %, respectively. Thus, the FeP/Fe₁-GO/Vis system is accompanied by the cycling of Fe³⁺ and Fe²⁺ during the TC degradation, which hinder the O₂[•] production.

Based on the above discussion, a plausible mechanism of FeP/Fe₁-GO/Vis/H₂O₂ system was proposed (Fig. 8). Firstly, under visible light irradiation, both FeP and Fe₁-GO are excited to generate hole (h⁺) in the valence band (VB) and electron (e⁻) in the conduction band (CB) on FeP and Fe₁-GO, respectively. The CB and VB for FeP and Fe₁-GO are -0.46 and 0.63 eV, -0.34 and 1.03 eV versus NHE, respectively. The photo-generated electrons are transferred with high efficiency from the CB of FeP to the CB of Fe₁-GO, the rapid recombination of photogenerated electron hole pairs can be effectively suppressed. Secondly, due to nice locally conjugated aromatic group in GO, a steady stream of electrons from the CB of Fe₁-GO further rapid transfer to the Fe single atoms through GO to activate H₂O₂ to generate HO[•] and O₂[•]. Because of rich Fe

single atoms at the GO surface, the electrons streams accelerate the redox reaction of Fe³⁺/Fe²⁺ cycles during H₂O₂ activation. Finally, the activation of H₂O₂ to generate HO[•] and following with the transformation of O₂[•], and these radicals give rise to the efficient TC degradation. At the same time, the holes on the VB of Fe₁-GO are migrated to that of FeP, and then the surface adsorbed OH/H₂O on catalyst will form a HO[•] using these holes. Finally, the TC was oxidized by these reactive oxygen species (ROS) owing to its strong oxidizing ability.

3.7. The pathway of TC degradation

Based on the intermediate products discovered by LC-TOF-MS, the degradation pathways of TC in the FeP/Fe₁-GO/Vis/H₂O₂ system were unraveled. In the FeP/Fe₁-GO/Vis/H₂O₂ system for the degradation of TC, the results of MS spectra are shown in Fig. S5. Based on the preceding analysis and researches [44,45], the degradation pathway of TC in the FeP/Fe₁-GO/Vis/H₂O₂ system was postulated in Fig. 9. The main degradation products were namely from P1 to P19. Combining these test products and related reports, two main pathways for the degradation process have been suggested. The cyclization of the OH group in pathway 1 allows the TC molecule to be transformed to P1-P4 at the C11a-C12 double bond location. TC molecules and intermediates degrade into lower molecular weight secondary metabolites when exposed to visible light for an extended period of time. In the presence of reactive chemicals (h⁺, HO[•] and O₂[•]), secondary products with lower molecular weight are formed when TC molecules and intermediates degrade. The pathway III was mainly a continuous fragmentation. Some larger molecular structures of P5-P8 may occur in the FeP/Fe₁-GO/Vis/H₂O₂ system, mostly because the O₂[•] and HO[•] species attack the TC benzene ring cooperatively, pushing the benzene ring to open its ring chain. Following that, the N-demethylation pathway creates secondary breakdown products with a reduced molecular weight, and then the oxidation of the formamide group, double bond can be obtained after the degradation products of smaller molecular weight tertiary degradation products. Finally, the products are ultimately decomposed into CO₂, H₂O, NH₄⁺ molecules and other intermediate products.

Additionally, using QSAR predictions made possible by the Toxicity Estimation Software Tool (TEST), the toxicity of TC and 19

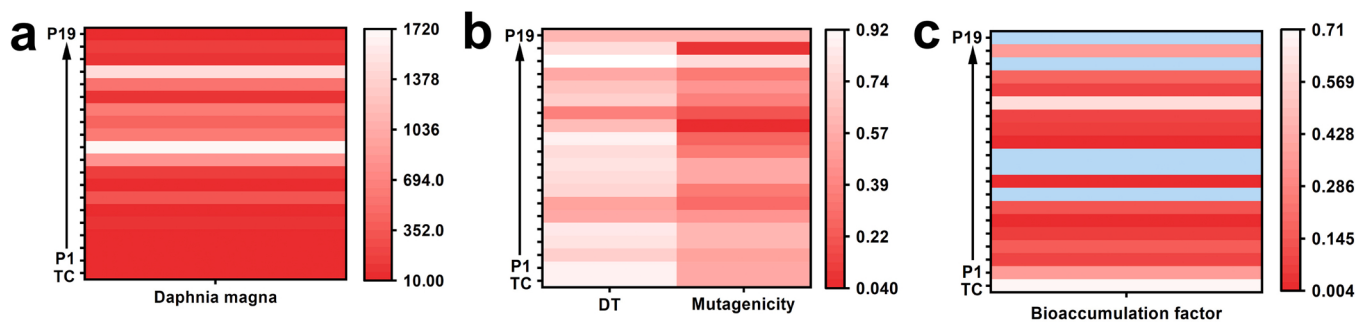


Fig. 10. (a) *Daphnia magna* LC₅₀ (48 h), (b) developmental toxicant (DT), mutagenicity positive and (c) bioaccumulation factor of TC and its intermediate products.

intermediates was investigated [46]. The toxicity of TC and its intermediates was evaluated by four evaluation indicators: *Daphnia magna* LC₅₀ (48 h), developmental toxicant (DT), mutagenicity positive and bioaccumulation factor. Fig. 10a shows that *Daphnia magna* LC₅₀ for TC was 12.7 mg/L. The *Daphnia magna* LC₅₀ values for all TC intermediates were higher than the TC. Fig. 10b shows the developmental toxicity and mutagenicity positive of TC and its intermediates. However, after FeP/Fe₁-GO/Vis/H₂O₂ system, a developmentally non-toxic and fifteen mutagenic-negative TC intermediates were produced. Interestingly, the bioaccumulation factors of all intermediates were lower than TC (Fig. 10c). According to the toxicity prediction results presented above, while some intermediates remain harmful, the total toxicity of these intermediates can be lowered by prolonging the reaction period.

4. Conclusions

In summary, a dual photo-functional of FeP/Fe₁-GO Fenton-like catalyst was constructed to active H₂O₂ for the degradation of antibiotic TC pollutants under visible light irradiation. Compared with single component of FeP and Fe₁-GO, the TC removal efficiency rate for the dual-photo-functional sites of FeP/Fe₁-GO exhibited 1.07 times higher than that of FeP and Fe₁-GO in sum. The most important finding is that the present FeP/Fe₁-GO/Vis/H₂O₂ system showed extremely stable and even after 100th cycle, the TC removal efficiency still kept around 93.6 %. Besides, the FeP/Fe₁-GO/Vis/H₂O₂ system also can bear a broad pH range (3–11), various common inorganic anions, and different water matrices ions conditions. The efficient electrons from excited FeP transfer to Fe₁-GO, and then flow to the single atom Fe sites to active H₂O₂ to generate radicals, resulting in the higher performance of TC removal. The photogenerated electrons stream from FeP and Fe₁-GO accelerate the Fe³⁺/Fe²⁺ cycles in Fe single atoms sites contribute the highly stable activity and long-term multiple recycles. This investigation gives us a route to design a highly stable Fenton-like catalyst via dual-photo-active sites together with single atoms strategy to cope with water treatments.

CRediT authorship contribution statement

Xiuying Li: Methodology, Data curation, Formal analysis, Writing – original draft. **Jiayue Hu:** Investigation, Methodology, Formal analysis, Writing – original draft. **Yuepeng Deng:** Methodology, Formal analysis. **Tong Li:** Supervision, Supervision. **Zhao-Qing Liu:** Methodology, Writing – review & editing. **Zhu Wang:** Conceptualization, Supervision, Writing – review & editing, Funding acquisition.

Declaration of Competing Interest

The authors declare that they have no known competing financial interests or personal relationships that could have appeared to influence the work reported in this paper.

Data availability

Data will be made available on request.

Acknowledgements

The authors gratefully acknowledge the support provided by NSFC (52070047), Guangdong Natural Science Foundation (2021A1515011898) and Guangzhou City Science and Technology Project (201904010217).

Appendix A. Supporting information

Supplementary data associated with this article can be found in the online version at doi:10.1016/j.apcatb.2022.122243.

References

- [1] L. Xu, H. Zhang, P. Xiong, Q. Zhu, C. Liao, G. Jiang, Occurrence, fate, and risk assessment of typical tetracycline antibiotics in the aquatic environment: a review, *Sci. Total Environ.* 753 (2021), 141975.
- [2] X. Chen, Y. Yang, Y. Ke, C. Chen, S. Xie, A comprehensive review on biodegradation of tetracyclines: Current research progress and prospect, *Sci. Total Environ.* (2022), 152852.
- [3] S. Shao, X. Wu, Microbial degradation of tetracycline in the aquatic environment: a review, *Crit. Rev. Biotechnol.* 40 (2020) 1010–1018.
- [4] B. Fan, Y. Tan, J. Wang, B. Zhang, Y. Peng, C. Yuan, C. Guan, X. Gao, S. Cui, Application of magnetic composites in removal of tetracycline through adsorption and advanced oxidation processes (AOPs): a review, *Processes* 9 (2021) 1644.
- [5] M. Gagol, A. Przyjazny, G. Boczkaj, Wastewater treatment by means of advanced oxidation processes based on cavitation—a review, *Chem. Eng. J.* 338 (2018) 599–627.
- [6] C.A. Lutterbeck, E.L. Machado, K. Kümmeler, Photodegradation of the antineoplastic cyclophosphamide: a comparative study of the efficiencies of UV/H₂O₂, UV/Fe²⁺/H₂O₂ and UV/TiO₂ processes, *Chemosphere* 120 (2015) 538–546.
- [7] N. Zheng, X. He, R. Hu, W. Guo, Z. Hu, Co-activation of persulfate by cation and anion from FeP for advanced oxidation processes, *Appl. Catal. B Environ.* 298 (2021), 120505.
- [8] B. Jain, A.K. Singh, H. Kim, E. Lichtfouse, V.K. Sharma, Treatment of organic pollutants by homogeneous and heterogeneous Fenton reaction processes, *Environ. Chem. Lett.* 16 (2018) 947–967.
- [9] S. Giannakis, M.I.P. López, D. Spuhler, J.A.S. Pérez, P.F. Ibáñez, C. Pulgarín, Solar disinfection is an augmentable, in situ-generated photo-Fenton reaction—part 1: a review of the mechanisms and the fundamental aspects of the process, *Appl. Catal. B Environ.* 199 (2016) 199–223.
- [10] Q. Ouyang, F. Kou, P.E. Tsang, J. Lian, J. Xian, J. Fang, Z. Fang, Green synthesis of Fe-based material using tea polyphenols and its application as a heterogeneous Fenton-like catalyst for the degradation of lincomycin, *J. Clean. Prod.* 232 (2019) 1492–1498.
- [11] H. Yu, J. Ji, Q. Yan, M. Xing, Transition metal phosphides for heterogeneous Fenton-like oxidation of contaminants in water, *Chem. Eng. J.* (2022), 137856.
- [12] C. Martínez-Sánchez, I. Robles, L. Godínez, Review of recent developments in electrochemical advanced oxidation processes: application to remove dyes, pharmaceuticals, and pesticides, *J. Environ. Sci. Technol.* (2022) 12611–12678.
- [13] H. Jin, X. Tian, Y. Nie, Z. Zhou, C. Yang, Y. Li, L. Lu, Oxygen vacancy promoted heterogeneous fenton-like degradation of ofloxacin at pH 3.2–9.0 by Cu substituted magnetic Fe₃O₄@FeOOH nanocomposite, *Environ. Sci. Technol.* 51 (2017) 12699–12706.
- [14] P. Fan, L. Li, Y. Sun, J. Qiao, C. Xu, X. Guan, Selenate removal by Fe(0) coupled with ferrous iron, hydrogen peroxide, sulfidation, and weak magnetic field: a comparative study, *Water Res.* 159 (2019) 375–384.

- [15] T. Li, Z. Wang, Z. Zhang, K. Feng, J. Liang, D. Wang, L. Zhou, Organic carbon modified Fe_2O_4 /schwertmannite for heterogeneous Fenton reaction featuring synergistic in-situ H_2O_2 generation and activation, *Sep. Purif. Technol.* 276 (2021).
- [16] L. Sun, X. Tan, W. Ding, Y. Huang, Emerging investigator series: hetero-phase junction 1T/2H- MoS_2 nanosheets decorated by FeOOH nanoparticles for enhanced visible light photo-Fenton degradation of antibiotics, *Environ. Sci. Nano* 9 (2022) 2342–2350.
- [17] P. Jiang, Q. Liu, Y. Liang, J. Tian, A.M. Asiri, X. Sun, A cost-effective 3D hydrogen evolution cathode with high catalytic activity: FeP nanowire array as the active phase, *Angew. Chem. Int. Ed.* 53 (2014) 12855–12859.
- [18] A. Yildiz, T. Chouki, A. Athi, M. Harb, S.W. Verbruggen, R. Ninakanti, S. Emin, Efficient iron phosphide catalyst as a counter electrode in dye-sensitized solar cells, *ACS Appl. Energy Mater.* 4 (2021) 10618–10626.
- [19] J.E. Katz, X. Zhang, K. Attenkofer, K.W. Chapman, C. Frandsen, P. Zarzycki, K. M. Rosso, R.W. Falcone, G.A. Waychunas, B. Gilbert, Electron small polarons and their mobility in iron (oxyhydr) oxide nanoparticles, *Science* 337 (2012) 1200–1203.
- [20] S.C. Shit, I. Mondal, S. Pendem, L. Bai, J.Y. Park, J. Mondal, MOF-derived bifunctional iron oxide and iron phosphide nanoarchitecture photoelectrode for neutral water splitting, *ChemElectroChem* 5 (2018) 2842–2849.
- [21] X. Wang, K. Chen, G. Wang, X. Liu, H. Wang, Rational design of three-dimensional graphene encapsulated with hollow FeP@carbon nanocomposite as outstanding anode material for lithium ion and sodium ion batteries, *ACS Nano* 11 (2017) 11602–11616.
- [22] L.S. Zhang, X.H. Jiang, Z.A. Zhong, L. Tian, Q. Sun, Y.T. Cui, X. Liu, J.P. Zou, S. L. Luo, Carbon nitride supported high-loading Fe single-atom catalyst for activation of peroxymonosulfate to generate ${}^1\text{O}_2$ with 100% selectivity, *Angew. Chem. Int. Ed.* 60 (2021) 21751–21755.
- [23] S. Lan, B. Jing, C. Yu, D. Yan, Z. Li, Z. Ao, M. Zhu, Prudent iron single-atom accelerated interfacial piezoelectric polarization for self-powered water motion triggered fenton-like reaction, *Small* 18 (2022) 2105279.
- [24] X. Wang, R. Yin, L. Zeng, M. Zhu, A review of graphene-based nanomaterials for removal of antibiotics from aqueous environments, *Environ. Pollut.* 253 (2019) 100–110.
- [25] S. Shi, C. Sun, X. Yin, L. Shen, Q. Shi, K. Zhao, Y. Zhao, J. Zhang, FeP quantum dots confined in carbon-nanotube-grafted p-doped carbon octahedra for high-rate sodium storage and full-cell applications, *Adv. Funct. Mater.* 30 (2020) 1909283.
- [26] Z. Zhang, C. Wu, Z. Chen, H. Li, H. Cao, X. Luo, Z. Fang, Y. Zhu, Spatially confined synthesis of a flexible and hierarchically porous three-dimensional graphene/FeP hollow nanosphere composite anode for highly efficient and ultrastable potassium ion storage, *J. Mater. Chem. A* 8 (2020) 3369–3378.
- [27] X. Dong, H. Yan, Y. Jiao, D. Guo, A. Wu, G. Yang, X. Shi, C. Tian, H. Fu, 3D hierarchical V–Ni-based nitride heterostructure as a highly efficient pH-universal electrocatalyst for the hydrogen evolution reaction, *J. Mater. Chem. A* 7 (2019) 15823–15830.
- [28] Y. Wu, Y. Wang, Z. Wang, X. Li, Highly dispersed CoP on three-dimensional ordered mesoporous FeP for efficient electrocatalytic hydrogen production, *J. Mater. Chem. A* 9 (2021) 23574–23581.
- [29] C. Yu, Y. Shi, F. Yan, Y. Zhao, C. Zhu, X. Zhang, X. Zhang, Y. Chen, Three-dimensional FeP nanotube arrays fabricated through electrostatic-repulsion-limited-nucleation strategy for high-efficiency hydrogen evolution, *Chem. Eng. J.* 423 (2021).
- [30] X.F. Lu, L. Yu, X.W. Lou, Highly crystalline Ni-doped FeP/carbon hollow nanorods as all-pH efficient and durable hydrogen evolving electrocatalysts, *Sci. Adv.* 5 (2019) eaav6009.
- [31] N. Maslekar, P.B. Zetterlund, P.V. Kumar, V. Agarwal, Mechanistic aspects of the functionalization of graphene oxide with ethylene diamine: implications for energy storage applications, *ACS Appl. Nano Mater.* 4 (2021) 3232–3240.
- [32] L. Gao, T. Ma, L. Zhang, X. Yang, Porous FeP@C frameworks as anode materials for high performance lithium ion capacitors, *J. Solid State Electrochem.* 25 (2021) 2055–2063.
- [33] J.-Y. Hu, Z. Li, C.-Y. Zhai, J.-F. Wang, L.-X. Zeng, M.-S. Zhu, Plasmonic photo-assisted electrochemical sensor for detection of trace lead ions based on Au anchored on two-dimensional g-C₃N₄/graphene nanosheets, *Rare Met.* 40 (2021) 1727–1737.
- [34] G. Yang, Y. Jiao, H. Yan, Y. Xie, A. Wu, X. Dong, D. Guo, C. Tian, H. Fu, Interfacial engineering of MoO_2 -FeP heterojunction for highly efficient hydrogen evolution coupled with biomass electrooxidation, *Adv. Mater.* 32 (2020) 2000455.
- [35] Y. Guo, P. Yuan, J. Zhang, H. Xia, F. Cheng, M. Zhou, J. Li, Y. Qiao, S. Mu, Q. Xu, Co₂P-CoN double active centers confined in n-doped carbon nanotube: heterostructural engineering for trifunctional catalysis toward HER, ORR, OER, and Zn-air batteries driven water splitting, *Adv. Funct. Mater.* 28 (2018) 1805641.
- [36] Y. Jia, L. Zhang, A. Du, G. Gao, J. Chen, X. Yan, C.L. Brown, X. Yao, Defect graphene as a trifunctional catalyst for electrochemical reactions, *Adv. Mater.* 28 (2016) 9532–9538.
- [37] Z. Xu, J. Hu, H. Dong, Y. Zhu, M. Zhu, Near-infrared light-assisted methanol oxidation reaction over the ferrous phosphide, *J. Colloid Interface Sci.* 626 (2022) 599–607.
- [38] W. Liu, P. Wang, J. Chen, X. Gao, H. Che, B. Liu, Y. Ao, Unraveling the mechanism on ultrahigh efficiency photocatalytic H_2O_2 generation for dual-heteroatom incorporated polymeric carbon nitride, *Adv. Funct. Mater.* 32 (2022) 2205119.
- [39] H. Che, P. Wang, J. Chen, X. Gao, B. Liu, Y. Ao, Rational design of donor-acceptor conjugated polymers with high performance on peroxydisulfate activation for pollutants degradation, *Appl. Catal. B Environ.* 316 (2022), 121611.
- [40] Y. Wen, J. Chen, X. Gao, H. Che, P. Wang, B. Liu, Y. Ao, Piezo-enhanced photocatalytic performance of ZnO nanorod array for pollutants degradation in dynamic water: Insight into the effect of velocity and inner flow field, *Nano Energy* 101 (2022), 107614.
- [41] J. Hu, Y. Chen, Y. Zhou, L. Zeng, Y. Huang, S. Lan, M. Zhu, Piezo-enhanced charge carrier separation over plasmonic Au-BiOBr for piezo-photocatalytic carbamazepine removal, *Appl. Catal. B Environ.* 311 (2022), 121369.
- [42] J. Hu, C. Yu, C. Li, S. Lan, L. Zeng, M. Zhu, Thickness-dependent piezo-photo-responsive behavior of ZnAl-layered double hydroxide for wastewater remediation, *Nano Energy* 101 (2022), 107583.
- [43] K. Fan, C. Yu, S. Cheng, S. Lan, M. Zhu, Metallic Bi self-deposited BiOCl promoted piezocatalytic removal of carbamazepine, *Surf. Interfaces* 26 (2021), 101335.
- [44] Y. Chen, R. Yin, L. Zeng, W. Guo, M. Zhu, Insight into the effects of hydroxyl groups on the rates and pathways of tetracycline antibiotics degradation in the carbon black activated peroxydisulfate oxidation process, *J. Hazard. Mater.* 412 (2021), 125256.
- [45] Y. Zhang, J. Zhou, X. Chen, L. Wang, W. Cai, Coupling of heterogeneous advanced oxidation processes and photocatalysis in efficient degradation of tetracycline hydrochloride by Fe-based MOFs: Synergistic effect and degradation pathway, *Chem. Eng. J.* 369 (2019) 745–757.
- [46] J. Zhang, C. Zhai, W. Zhao, Y. Chen, R. Yin, L. Zeng, M. Zhu, Insight into combining visible-light photocatalysis with transformation of dual metal ions for enhancing peroxymonosulfate activation over dibismuth copper oxide, *Chem. Eng. J.* 397 (2020), 125310.